VNU Journal of Science: Mathematics – Physics, Vol. 41, No. 1 (2025) 69-80

VNU Journal of Science: Mathematics - Physics

Journal homepage: https://js.vnu.edu.vn/MaP

Original Article

Optical Simulations of Organic Solar Cells with PBDB-T:ITIC and PTB7:$PC_{71}BM$ Photoactive Layers

Nguyen Duc Cuong*, Than Thi Thu Ha, Hoang Thi Hoa, Vu Thi Thao, Nguyen Tuan Canh, Nguyen Phuong Hoai Nam

VNU University of Engineering and Technology, 144 Xuan Thuy, Cau Giay, Hanoi, Vietnam

Received 21st December 2024
Revised 6th February 2025; Accepted 20th February 2025

Abstract: In this work, we present a comprehensive optical simulation analysis of bulk-heterojunction (BHJ) organic solar cells where PBDB-T:ITIC incorporated with PTB7:$PC_{71}BM$ blends served as photoactive layers. The simulations were performed using transfer matrix method implemented through a MATLAB script that is developed by McGehee's research group at Stanford University. This method involves calculating the optical transmission and reflection at each interface within the multilayer stack, as well as the attenuation of light within each layer. A comparative evaluation was conducted for solar cells employing these active layers in both conventional and inverted configurations, with a focus on key performance metrics including light-harvesting efficiency (LHE), exciton generation rate within the active layer ($G_{\mathrm{AL}}(x,\lambda)$), and the maximum achievable short-circuit current density ($J_{\mathrm{SC\text{-}max}}$). The obtained results showed that for both types of active layers, the inverted structure achieves a larger $J_{\mathrm{SC\text{-}max}}$ compared to the conventional structure. Additionally, the PBDB-T:ITIC-based absorber outperforms the PTB7:$PC_{71}BM$-based absorber in terms of $J_{\mathrm{SC\text{-}max}}$.

Keywords: Organic solar cells, optical simulations.

1. Introduction

Highly efficient organic solar cells (OSCs) are predominantly based on blends of electron-donor materials and fullerene-based electron-acceptor materials (fullerene acceptors, FAs) to form bulk heterojunctions (BHJs) within the devices. However, non-fullerene acceptors (NFAs) have become a principal focus of research in the development of BHJ OSCs due to their numerous advantageous properties [1]. Since 2015, concerted materials synthesis and device optimization efforts have improved

* Corresponding author.
E-mail address: cuongnd@vnu.edu.vn

https://doi.org/10.25073/2588-1124/vnumap.4980

the power conversion efficiencies (PCEs) for NFA OSCs from 6% to larger 13% [2, 3], thus outperforming their fullerene counterparts (which have PCEs <13%) [4, 5].

3,9-bis(2-methylene-(3-(1,1-dicyanomethylene)-indanone))-5,5,11,11-tetrakis(4-hexylphenyl)-dithieno[2,3-d:2',3'-d']-s-indaceno[1,2-b:5,6-b']dithiophene (ITIC) marks the advent of a new generation of small-molecule NFAs for OSCs. The energy levels of ITIC are well-aligned with low band-gap conducting polymers, enhancing charge separation efficiency and minimizing energy loss. ITIC molecules exhibit strong and broad absorption characteristics spanning from the visible to the near-infrared regions of the electromagnetic spectrum, with a peak absorption at 700 nm [6]. This broad absorption potential increases the overall light-harvesting capability of OSC devices, thereby improving PCEs. These attributes have established ITIC as the first small molecule electron acceptor to surpass the performance of the leading fullerene acceptor [6,6]-Phenyl-C71-butyric acid methyl ester ($PC_{71}BM$) in OSC devices fabricated under controlled conditions, such as in a glove box. When paired with Poly[(2,6-(4,8-bis(5-(2-ethylhexyl)thiophen-2-yl)-benzo[1,2-b:4,5-b']dithiophene))-alt-(5,5-(1',3'-di-2-thienyl-5',7'-bis(2-ethylhexyl)benzo[1',2'-c:4',5'-c']dithiophene-4,8-dione)] (PBDB-T) in an inverted-architecture device, ITIC achieved a PCE exceeding 11%, compared to a PCE of less than 8% when $PC_{71}BM$ was utilized as the electron acceptor [6]. This result originates from the broader absorption spectrum and more suitable energy level alignment of PBDB-T:ITIC compared to PBDB-T:$PC_{71}BM$. As reported in [6], during the exciton dissociation process in a BHJ blend film, electrons transition from the lowest unoccupied molecular orbital (LUMO) of the donor to the LUMO of the acceptor, while holes migrate from the highest occupied molecular orbital (HOMO) of the acceptor to the HOMO of the donor. The energy gap $\Delta_{\mathrm{LUMO}} = \mathrm{LUMO}_{\mathrm{donor}} - \mathrm{LUMO}_{\mathrm{acceptor}}$ in the PBDB-T:ITIC blend is 0.2 eV smaller than that in the PBDB-T:$PC_{71}BM$ blend, while the energy gap $\Delta_{\mathrm{HOMO}} = \mathrm{HOMO}_{\mathrm{donor}} - \mathrm{HOMO}_{\mathrm{acceptor}}$ in the PBDB-T:ITIC blend is 0.45 eV smaller than in the PBDB-T:$PC_{71}BM$ blend. These reductions play a crucial role in minimizing energy loss during exciton dissociation when transitioning from the PBDB-T:$PC_{71}BM$ to the PBDB-T:ITIC system. On the other hand, $PC_{71}BM$ is more compatible with Poly [[4,8-bis[(2-ethylhexyl)oxy]benzo[1,2-b:4,5-b']dithiophene-2,6-diyl][3-fluoro-2-[(2-ethylhexyl)carbonyl] thieno[3,4-b]thiophenediyl]] (PTB7) than ITIC. The absorption spectra of ITIC and PTB7 overlap significantly, preventing the advantages of ITIC from being fully realized when blended with PTB7. Typical reported PCEs of high-performance PTB7:$PC_{71}BM$ organic solar cells are 8.24% for the conventional structure and 9.214% for the inverted structure [7].

It is well-established that the working mechanism of BHJ OSCs involves four primary steps: i) Exciton generation; ii) Exciton diffusion; iii) Exciton dissociation into free electron and hole; and iv) Charge transport and collection [1]. In this work, to elucidate the efficiency of the initial step in the working mechanism of OSCs utilizing FAs and NFAs, we selected two representative blends: PBDB-T:ITIC and PTB7:$PC_{71}BM$. These blends were subjected to comparative analysis through optical simulations. Both conventional and inverted structures were employed, and their optical performances were compared, including the exciton generation rate within the active layer (G_{AL}), light-harvesting efficiency (LHE), and the maximum short-circuit current ($J_{\mathrm{SC\text{-}max}}$).

2. Simulation Model

Optical constants are fundamental parameters that describe how materials interact with electromagnetic waves, particularly with light. The primary optical constants are the refractive index (n) and the extinction coefficient (k). The refractive index ($n = \frac{c}{v}$) indicates how much light is bent, or refracted, as it enters the material, while the extinction coefficient (k) represents the degree of light absorption within the material [8]. Together, these constants define the complex refractive index, $\tilde{n} =$

$n + ik$, which influences how light propagates, reflects, and absorbs in various media. Optical constants are critical in fields such as optics, material science, and photonics for understanding and designing optical devices such as solar cells. Typically, the wavelength-dependent values of *n* and *k* are derived through ellipsometric analysis of thin-film materials [9]. Ellipsometry is a powerful, non-destructive optical technique that enables precise characterization of the optical constants by measuring changes in the polarization state of reflected or transmitted light. The amplitude ratio ψ and phase difference Δ between *p*- and *s*-polarized light waves were directly acquired from experimental measurements. Subsequently, the optical constants (refractive index *n* and extinction coefficient *k*) were determined by applying an optical model appropriate to the sample under investigation. This method is especially valuable for thin films, as it provides insights into layer thickness, surface morphology, and optical properties essential for applications in materials science and photonics.

Optical simulations of stacked-structure OSCs were conducted using a modified MATLAB script developed by the McGehee group at Stanford University [10, 11]. In this MATLAB script, the transfer matrix method was employed to compute transmission and reflection at each interface within the stack, alongside the attenuation in each layer [12, 13]. These calculations are grounded in the optical constants of the constituent materials, ensuring accurate modeling of light interactions across interfaces and within layers. In this work, the stacked structure and thickness of each layer in both conventional and inverted OSCs, utilizing two types of active layers (AL), are as follows:

Conventional structure:

ITO(160nm)/PEDOT:PSS(40nm)/AL(varying thickness)/LiF(1nm)/Al(120nm).

Inverted structure:

ITO(160nm)/ZnO(50nm)/AL(varying thickness)/MoO_3(10nm)/Ag(120nm).

In both configurations, the devices are illuminated from the indium tin oxide (ITO) side, with the metal electrodes (aluminum and silver) functioning as reflectors. The optical constant database for the PBDB-T:ITIC and PTB7:$PC_{71}BM$ organic blends AL is sourced from the works by Kerremans et al., and Stelling et al., respectively [14, 15]. In these studies, the weight ratios of 1:1 and 1:1.6 were employed for PBDB-T:ITIC and PTB7:$PC_{71}BM$ organic blends, respectively. Wavelength-dependent optical constants (*n*, *k*) for each material as shown in Fig. 1, including ITO, Poly(3,4-ethylenedioxythiophene):Polystyrene sulfonate (PEDOT:PSS), lithium fluoride (LiF), zinc oxide (ZnO), molybdenum oxide (MoO_3), aluminum (Al), silver (Ag), organic blends (PBDB-T:ITIC and PTB7:$PC_{71}BM$) were compiled into a single Excel file, which served as input data for the MATLAB script. Additionally, the script incorporated the names of materials constituting the cell structure along with their corresponding thicknesses (in nanometers). The standard solar irradiation spectrum data (AM1.5 Global) $\Phi(\lambda)$, which has an integrated power of 100 mW/cm^2, were also included. Simulations were conducted over a wavelength range of 300 to 800 nm. The output data from the calculations comprised internal optical electric field ($E_j(x,\lambda)$), exciton generation rate within the active layer ($G_{\mathrm{AL}}(x,\lambda)$), light-harvesting efficiency (LHE(λ)), and maximum short-circuit current ($J_{\mathrm{SC\text{-}max}}$).

The exciton generation rate at position *x* within layer *j* at a specific wavelength λ was calculated according to [12]:

$$G_j(x,\lambda) = \frac{\lambda}{hc} Q_j(x,\lambda) \tag{1}$$

where $Q_j(x,\lambda) = \frac{4\pi c\varepsilon_0 n_j k_j}{2\lambda}\left|E_j(x,\lambda)\right|^2$ is the time average of the energy dissipated per second in layer *j* at position *x* at normal incidence, *c* is the speed of light, ε_0 is the permittivity of free space, and $E_j(x,\lambda)$ is the internal optical electric field.

The position-dependent exciton generation rate ($G_{\mathrm{AL}}(x)$) within the active layer was determined by integrating over the entire desired wavelength range:

$$G_{\mathrm{AL}}(x) = \int_{\lambda_{\min}}^{\lambda_{\max}} G_{\mathrm{AL}}(x,\lambda)d\lambda \quad (2)$$

The wavelength-dependent light-harvesting efficiency (LHE(λ)) was calculated according to:

$$\mathrm{LHE}(\lambda) = \frac{N_{\text{exciton in AL}}}{N_{\text{photon}}} = \frac{\int_0^{d_{\mathrm{AL}}} G_{\mathrm{AL}}(x,\lambda)dx}{\Phi(\lambda).\frac{\lambda}{hc}} \quad (3)$$

where $N_{\text{exciton in AL}}$ and N_{photon} are the numbers of excitons generated within the active layer and the number of incident photons in a unit of time, respectively. d_{AL} is the thickness of the active layer.

Assuming that the efficiency of all subsequent steps following exciton generation is 100%, the maximum short-circuit current $J_{\text{SC-max}}$ was calculated according to:

$$J_{\text{SC-max}} = e\int_0^{d_{\mathrm{AL}}} G_{\mathrm{AL}}(x)dx \quad (4)$$

Notably, this value is invariably higher than the short-circuit current (J_{SC}) achievable in an actual organic solar cell with the same configuration. This discrepancy arises from the unavoidable losses during exciton diffusion, exciton dissociation, and charge transport and collection processes.

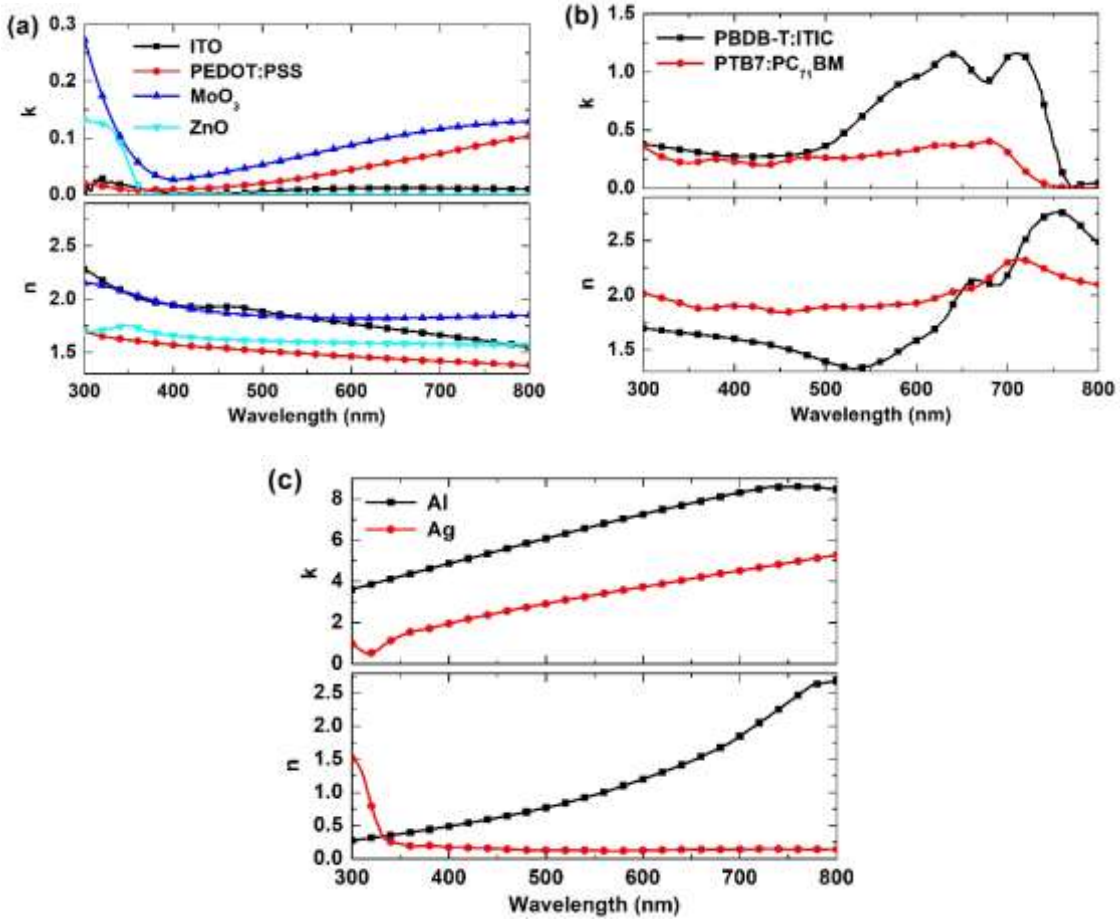

Figure 1. Wavelength-dependent optical constants (*n*, *k*) of (a) ITO, PEDOT:PSS (CLEVIOS P VP AI 4083), MoO_3, ZnO; (b) PBDB-T:ITIC and PTB7:PC_{71}BM organic blends, and (c) Ag and Al [14, 15]. The data of LiF are not shown.

Table 1. Semiconductor physical parameters of the materials constituting the organic solar cells.

Material / Parameter	PEDOT:PSS	MoO_3	ZnO	PBDB-T:ITIC	PTB7:$PC_{71}BM$
d (nm)	40	10	50	0–250	0–250
E_g (eV)	2.786	3.0	3.4	1.2	1.05
χ (eV)	2.2	2.5	4.25	4.03	4.1
μ_e ($cm^2 \cdot V^{-1} \cdot s^{-1}$)	1×10^{-5}	25	50	3.1×10^{-4}	5.1×10^{-4}
μ_h ($cm^2 \cdot V^{-1} \cdot s^{-1}$)	3.2×10^{-4}	100	20	3.2×10^{-4}	5.2×10^{-4}
References	[16]	[17]	[18–20]	[6, 16, 21, 22]	[6, 16, 21, 22]

3. Results and Discussion

As discussed in the Introduction, the initial stage in the operational mechanism of an organic solar cell involves photon absorption and exciton generation. When photons are absorbed within the active layer, excitons are formed, and their generation rates vary across different spatial positions within this layer. Achieving high LHE and an optimal exciton generation rate profile is essential for the development of high-performance solar cells.

Subsequent stages involve the diffusion of excitons to the donor-acceptor interface, where they dissociate to produce charge carriers: electrons at the LUMO of the acceptor material and holes at the HOMO of the donor material. These charge carriers are then transported through the respective donor and acceptor networks before being collected at the corresponding electrodes. The semiconductor physical parameters, including energy bandgap, electron affinity, and charge carrier mobilities of the materials comprising the organic solar cells, are summarized in Table 1. The organic blends are modeled as single semiconductor layers, with the bandgap (E_g) defined by the energy difference between the HOMO level of the donor materials (PBDB-T, PTB7) and the LUMO level of the acceptor materials (ITIC, $PC_{71}BM$).

Due to the inherently low charge carrier mobility of organic materials (see Table 1), the active layer is typically kept relatively thin (100–200 nm). A uniform exciton generation rate within the active layer facilitates efficient charge carrier transport and collection, contributing to an increased short-circuit current density (J_{SC}) and, consequently, an improved PCE.

The wavelength-dependent LHE spectra for varying thicknesses of the active layer are presented in Fig. 2. Figures 2(a) and 2(c) demonstrate that for the PBDB-T:ITIC blend, notable variations in LHE with different active layer thicknesses are evident in the wavelength ranges of 350–550 nm and 700–770 nm. Conversely, the LHE curves for the PTB7:PC71BM blend exhibit distinctions across the entire wavelength spectrum, as illustrated in Figs. 2(b) and 2(d). As denoted in a previous study by Zhao et al., the absorption spectrum of the PBDB-T is complementary with that of ITIC, such that the onset of extinction coefficient *k* for the PBDB-T:ITIC blend, as shown in Fig. 1, and consequently the onset of LHE in Figs, 2(a) and 2(c), is determined by the onset at approximately 770 nm in the absorption spectrum of ITIC [6]. The absorption spectrum onset of PTB7:$PC_{71}BM$ is determined by the absorption edge of the PTB7 polymer, at approximately 750 nm [23], which is consistent with the $k(\lambda)$ and LHE spectra. Therefore, it can be concluded that the broader LHE spectrum of the PBDB-T:ITIC blend, in comparison with PTB7:$PC_{71}BM$, originates from its broader absorption and $k(\lambda)$ spectra. Additionally, due to the lower extinction coefficient of the PTB7:$PC_{71}BM$ blend, a thicker active layer is necessary to achieve a LHE comparable to that of PBDB-T:ITIC blend. Figure 3 illustrates the dependence of average LHE values, measured over the wavelength range from 300 to 800 nm, on the thickness of the active

layer. The obtained results indicate that for PBDB-T:ITIC absorber, the inverted structure yields higher LHE when the active layer thickness exceeds 120 nm. For PTB7:$PC_{71}BM$ absorber, the inverted structure demonstrates higher LHE when the active layer thickness ranges between 130 nm and 240 nm. This phenomenon can be attributed to the higher and broader transmittance spectrum (lower k value) of the wide-bandgap semiconductor material ZnO ($E_g = 3.4$ eV) in an inverted structure, as compared to PEDOT:PSS ($E_g = 2.786$ eV) in a conventional structure (see Table 1).

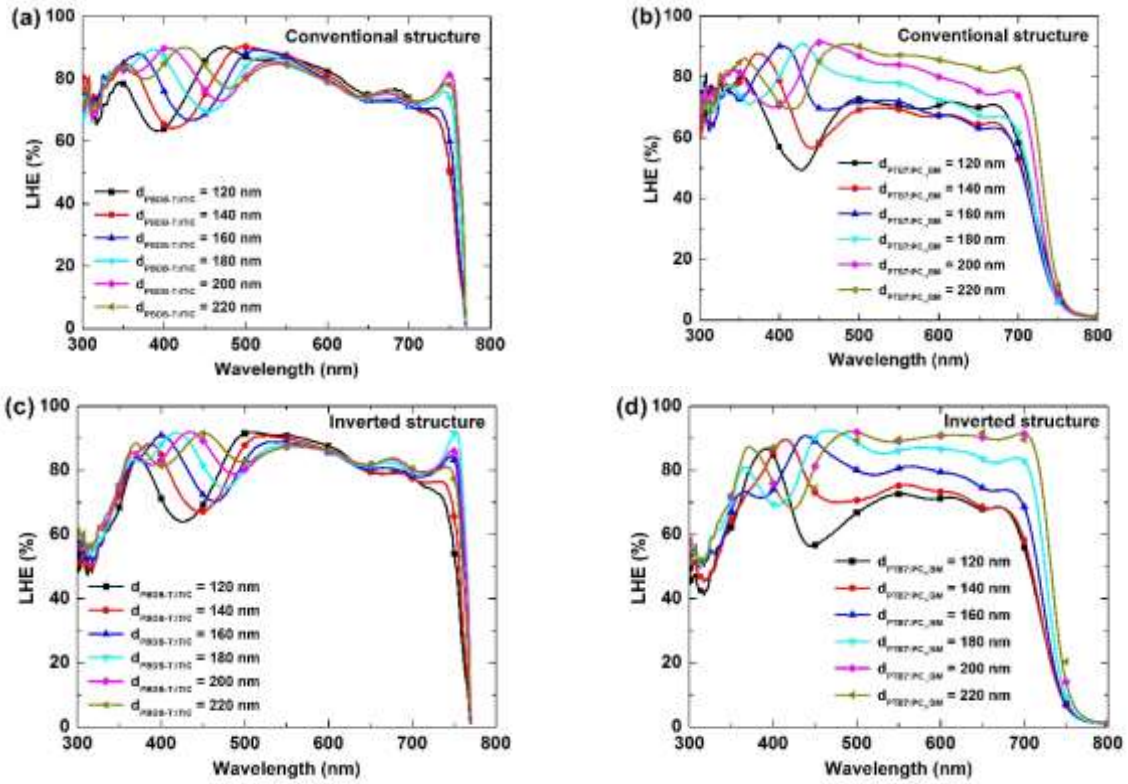

Figure 2. The variation of light-harvesting efficiency (LHE) within the active layer with the thickness of PBDB-T:ITIC and PTB7:$PC_{71}BM$ active layers in organic solar cells with conventional structure (a, b) and inverted structure (c, d).

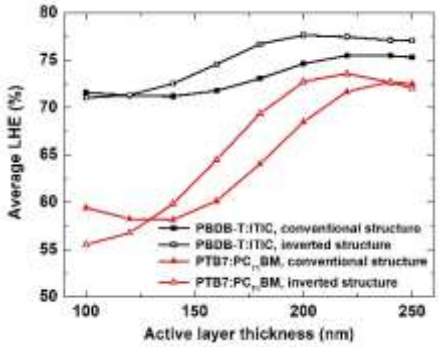

Figure 3. The dependence of average light-harvesting efficiency (LHE) on the thickness of PBDB-T:ITIC and PTB7:$PC_{71}BM$ active layers for two structures.

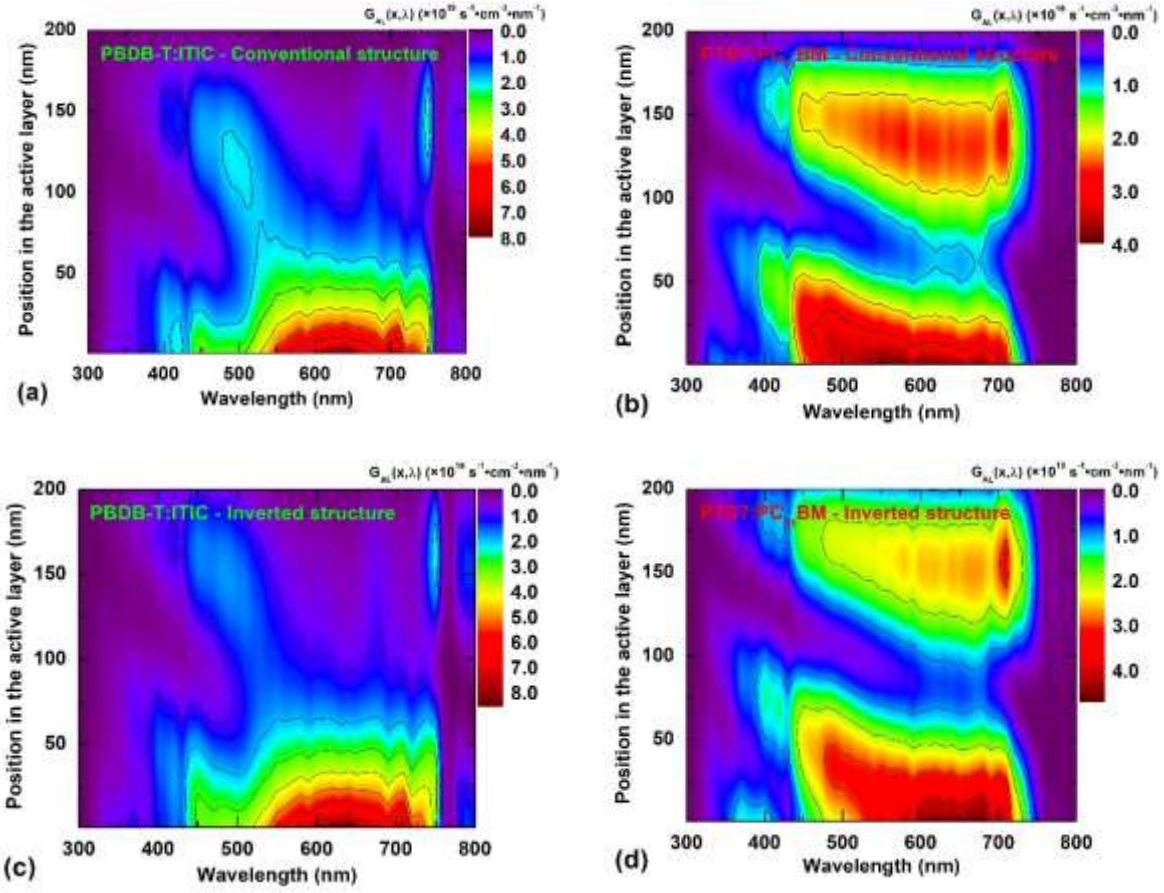

Figure 4. Position-dependent exciton generation rate at various wavelengths $G_{\mathrm{AL}}(x,\lambda)$ (see Equation 1) within the PBDB-T:ITIC and PTB7:PC_{71}BM active layers in organic solar cells with conventional structure (a,b) and inverted structure (c,d).

Fig. 4 presents the position-dependent exciton generation rate at various wavelengths $G_{\mathrm{AL}}(x,\lambda)$ within the active layer for organic solar cells featuring PBDB-T:ITIC (200 nm) and PTB7:PC_{71}BM (200 nm) active layers. For devices incorporating a PBDB-T:ITIC active layer, the maximum values of $G_{\mathrm{AL}}(x,\lambda)$ are achieved at a wavelength of 640 nm, for both conventional and inverted structures. Specifically, the conventional structure exhibits a peak $G_{\mathrm{AL}}(x,\lambda)$ value of $7.746 \times 10^{19}\ \mathrm{s^{-1} \cdot cm^{-3} \cdot nm^{-1}}$, while the inverted structure reaches a peak $G_{\mathrm{AL}}(x,\lambda)$ value of $8.566 \times 10^{19}\ \mathrm{s^{-1} \cdot cm^{-3} \cdot nm^{-1}}$. In the case of the PTB7:PC_{71}BM active layer, the conventional structure demonstrates the highest $G_{\mathrm{AL}}(x,\lambda)$ of $3.906 \times 10^{19}\ \mathrm{s^{-1} \cdot cm^{-3} \cdot nm^{-1}}$ at a wavelength of 550 nm, whereas the inverted structure achieves its peak $G_{\mathrm{AL}}(x,\lambda)$ of $4.717 \times 10^{19}\ \mathrm{s^{-1} \cdot cm^{-3} \cdot nm^{-1}}$ at a wavelength of 680 nm. In both scenarios, these maxima are observed at the front interfaces of the photoactive layers. For the PBDB-T:ITIC active layer, $G_{\mathrm{AL}}(x,\lambda)$ decreases substantially at positions x greater than 100 nm for both structures. In contrast, the exciton generation rate profile versus position in the PTB7:PC_{71}BM active layer exhibits two distinct regions: one from 0 to 75 nm and another from approximately 100 nm to 190 nm. This characteristic is distinctly illustrated in Fig. 5: the position-dependent exciton generation rate $G_{\mathrm{AL}}(x)$ (see Equation 3) for PBDB-T:ITIC active layer demonstrates an almost monotonic decrease with

increasing position x at varying thickness (Figs. 5a and 5c). In contrast, the $G_{\mathrm{AL}}(x)$ profile for PTB7:$PC_{71}BM$ active layer exhibits a wave-like behavior with position x, particularly pronounced in thicker active layers (Figs. 5b and 5d). The distinct behavior of exciton generation rates between PBDB-T:ITIC and PTB7:$PC_{71}BM$ active layers suggests that a relatively thin PBDB-T:ITIC blend layer is sufficient to achieve a high exciton generation rate, whereas a thicker PTB7:$PC_{71}BM$ blend layer is necessary to produce a comparable exciton generation rate. Additionally, the limited charge mobilities in organic blends contribute to inefficient charge transport in thicker active layers (see Table 1). This phenomenon partially accounts for the lower efficiency of solar cells utilizing PTB7:$PC_{71}BM$ as the absorber compared to those using PBDB-T:ITIC absorber.

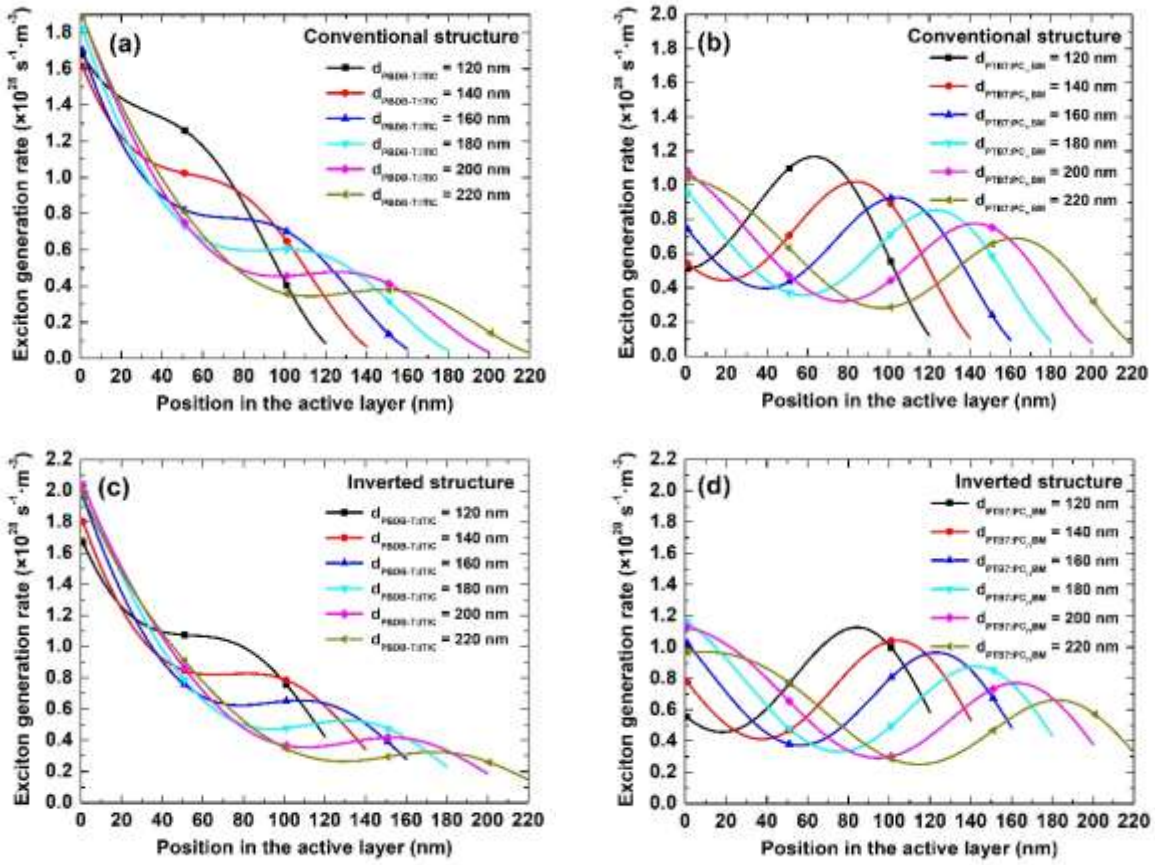

Figure 5. The variation of exciton generation rates $G_{\mathrm{AL}}(x)$ within the active layer (AL) as a function of position x in the active layer with varying thicknesses of PBDB-T:ITIC and PTB7:$PC_{71}BM$ ALs in conventional structure (a, b) and inverted structure (c, d).

Fig. 6 depicts the relationship between the $J_{\text{SC-max}}$ obtained through optical simulations and the thickness of active layers in conventional- and inverted-structure solar cells. Generally, the PTB7:$PC_{71}BM$ active layer yields a smaller $J_{\text{SC-max}}$ compared to the PBDB-T:ITIC active layer across all thicknesses and for both structures. For both absorbers, the inverted structure results in a higher $J_{\text{SC-max}}$, attributable to the higher LHE and $G_{\mathrm{AL}}(x)$ previously mentioned.

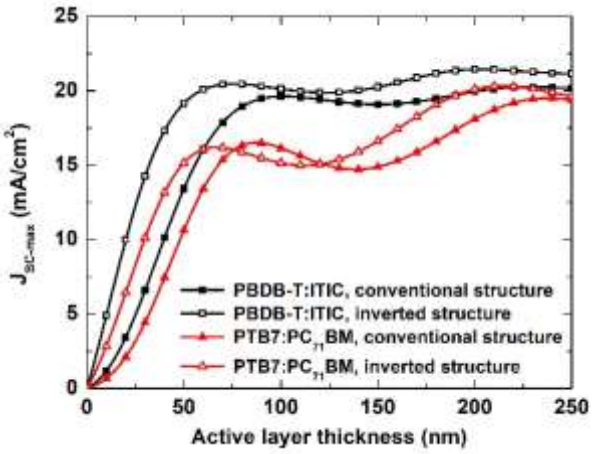

Figure 6. The dependence of maximum short-circuit current obtained through optical simulations ($J_{SC\text{-}max}$) on the thickness of PBDB-T:ITIC and PTB7:$PC_{71}BM$ active layers for two structures.

Table 2. The maximum short-circuit current ($J_{SC\text{-}max}$) values obtained from optical simulations for conventional and inverted structure organic solar cells at varying thicknesses of the PBDB-T:ITIC active layer. The peak values and their corresponding thicknesses are highlighted in bold

PBDB-T:ITIC thickness (nm)	$J_{SC\text{-}max}$ (mA/cm^2)	
	Conventional structure	Inverted structure
90	19.463	20.307
100	19.621	20.121
110	19.567	19.960
120	19.416	19.873
140	19.124	20.018
160	19.122	20.546
180	19.467	21.155
200	19.942	21.435
203	20.003	**21.439**
220	20.223	21.347
229	**20.250**	21.268
240	20.223	21.187

Tables 2 and 3 present the $J_{SC\text{-}max}$values for various active layer thicknesses in both structural configurations. For the PBDB-T:ITIC active layer, $J_{SC\text{-}max}$ reaches a maximum value of 20.25 mA/cm^2 at $d_{AL} = 229$ nm in the conventional structure, and 21.439 mA/cm^2 at $d_{AL} = 203$ nm in the inverted structure (Table 2). For the PTB7:$PC_{71}BM$ active layer, a peak value of $J_{SC\text{-}max} = 19.494$ mA/cm^2 is achieved at $d_{AL} = 238$ nm in the conventional structure, while the inverted structure provides a higher value of $J_{SC\text{-}max} = 20.136$ mA/cm^2 at a thinner active layer, specifically at $d_{AL} = 214$ nm (Table 3).

It should also be noted that experimental studies often employ significantly thinner active layers. For instance, an experimental short-circuit current density of 15.45 mA/cm² was reported for a similar conventional device structure: ITO/PEDOT/PTB7:$PC_{71}BM$(110 nm)/LiF/Al [24]. This value is slightly lower than the simulated value of 15.62 mA/cm² at a PTB7:$PC_{71}BM$ active layer thickness of 110 nm predicted in this study. In another study by Yao et al., [25], a conventional structure of

ITO/PEDOT/PBDB-T:ITIC(110 nm)/PFN-Br/Al exhibited an experimental short-circuit current density of 17 mA/cm², which corresponds to 86.88% of the simulated value in this study. Due to the relatively low charge carrier mobilities in organic compounds, which are approximately in the range of 1×10^{-4} to 1×10^{-3} $\mathrm{cm^2 \cdot V^{-1} \cdot s^{-1}}$ for PBDB-T:ITIC and PTB7:PC_{71}BM blends [2, 25, 26], employing a thicker active layer results in reduced carrier extraction efficiency. This inefficiency in charge transport directly contributes to the diminished performance of organic solar cells.

Table 3. The maximum short-circuit current ($J_{SC\text{-}max}$) values obtained from optical simulations for conventional and inverted structure organic solar cells at varying thicknesses of the PTB7:PC_{71}BM active layer. The peak values and their corresponding thicknesses are highlighted in bold

PTB7:PC_{71}BM thickness (nm)	$J_{SC\text{-}max}$ (mA/cm^2)	
	Conventional structure	Inverted structure
90	16.490	15.477
100	16.150	15.141
110	15.621	14.987
120	15.128	15.064
140	14.721	15.910
160	15.289	17.426
180	16.596	19.045
200	18.102	20.105
214	18.935	**20.316**
220	19.186	20.284
238	**19.494**	19.922
240	19.490	19.871

4. Conclusions

In summary, optical simulations of organic solar cells were conducted utilizing the transfer matrix method. The results consistently demonstrated that the inverted structure yielded higher short-circuit current densities. Within the same structural configuration, devices incorporating a PBDB-T:ITIC active layer exhibited higher short-circuit current densities compared to those with a PTB7:PC_{71}BM active layer. For the PBDB-T:ITIC active layer, the $J_{SC\text{-}max}$ were of 20.25 mA/cm^2 and 21.439 mA/cm^2 for conventional and inverted structures, respectively. In the case of PTB7:PC_{71}BM active layer, the maximum values of $J_{SC\text{-}max}$ were of 19.494 mA/cm^2 for the conventional structure and 20.316 mA/cm^2 for the inverted structures. Although these values represent ideal conditions and are significantly higher than experimental values, they provide valuable guidelines for selecting appropriate device configurations. This includes determining the optimal weight ratio of components in organic blends, as well as the thickness of the organic blend layer and other charge transport layers. Furthermore, the exciton generation rates calculated by the transfer matrix method are crucial input data for electrical simulation tools, such as SCAPS-1D, enabling a more comprehensive understanding of the performance of planar solar cells in general, and specifically organic solar cells.

Acknowledgments

This research was funded by the research project QG.23.33 of Vietnam National University, Hanoi.

References

[1] C. Yan et al., Non-fullerene Acceptors for Organic Solar Cells, Nat. Rev. Mater., Vol. 3, 2018, pp. 1-19, https://doi.org/10.1038/natrevmats.2018.3.

[2] W. Zhao et al., Molecular Optimization Enables Over 13% Efficiency in Organic Solar Cells, J. Am. Chem. Soc., Vol. 139, No. 21, 2017, pp. 7148-7151, https://doi.org/10.1021/jacs.7b02677.

[3] Y. Cui et al., Fine-Tuned Photoactive and Interconnection Layers for Achieving Over 13% Efficiency in a Fullerene-Free Tandem Organic Solar Cell, J. Am. Chem. Soc., Vol. 139, No. 21, 2017, pp. 7302-7309, https://doi.org/10.1021/jacs.7b01493.

[4] M. Li et al., Solution-processed Organic Tandem Solar Cells with Power Conversion Efficiencies >12%, Nat. Photonics, Vol. 11, No. 2, 2017, pp. 85-90, https://doi.org/10.1038/nphoton.2016.240.

[5] T. Kumari, S. M. Lee, S. H. Kang, S. Chen, C. Yang, Ternary Solar Cells with A Mixed Face-on and Edge-on Orientation Enable An Unprecedented Efficiency of 12.1%, Energy Environ. Sci., Vol. 10, No. 1, 2017, pp. 258-265, https://doi.org/10.1039/c6ee02851a.

[6] W. Zhao et al., Fullerene-Free Polymer Solar Cells with Over 11% Efficiency and Excellent Thermal Stability, Adv. Mater., Vol. 28, No. 23, 2016, pp. 4734-4739, https://doi.org/10.1002/adma.201600281.

[7] Z. He, C. Zhong, S. Su, M. Xu, H. Wu, Y. Cao, Enhanced Power-conversion Efficiency in Polymer Solar Cells Using An Inverted Device Structure, Nat. Photonics, Vol. 6, No. 9, 2012, pp. 591-595.

[8] S. O. Kasap, Principles of Electronic Materials and Devices, 4th Edition, McGraw-Hill Education, 2017, pp. 890-894.

[9] H. Fujiwara, Spectroscopic Ellipsometry: Principles and Applications, John Wiley & Sons, 2007.

[10] G. F. Burkhard, E. T. Hoke, Transfer Matrix Optical Modeling, McGehee Group (Stanford Univ). 2011, Available online: http://web.stanford.edu/group/mcgehee/transfermatrix/index.html (accessed on: May 15th, 2024).

[11] G. F. Burkhard, E. T. Hoke, M. D. McGehee, Accounting for Interference, Scattering, and Electrode Absorption to Make Accurate Internal Quantum Efficiency Measurements in Organic and Other Thin Solar Cells, Adv. Mater., Vol. 22, No. 30, 2010, pp. 3293-3297, https://doi.org/10.1002/adma.201000883.

[12] L. A. A. Pettersson, L. S. Roman, O. Inganäs, Modeling Photocurrent Action Spectra of Photovoltaic Devices Based on Organic Thin Films, J. Appl. Phys., Vol. 86, 1999, pp. 487-496, https://doi.org/10.1063/1.370757.

[13] P. Peumans, A. Yakimov, S. Forrest, Small Molecular Weight Organic Thin-Film Photodetectors and Solar Cells, J. Appl. Phys., Vol. 93, 2003, pp. 3693-3723, https://doi.org/10.1063/1.1534621.

[14] R. Kerremans, C. Kaiser, W. Li, N. Zarrabi, P. Meredith, A. Armin, The Optical Constants of Solution-Processed Semiconductors—New Challenges with Perovskites and Non-Fullerene Acceptors, Adv. Opt. Mater., Vol. 8, No. 16, 2020, pp. 2000319, https://doi.org/10.1002/adom.202000319.

[15] C. Stelling, C. R. Singh, M. Karg, T. A. F. König, M. Thelakkat, M. Retsch, Plasmonic Nanomeshes: Their Ambivalent Role As Transparent Electrodes In Organic Solar Cells, Sci. Rep., Vol. 7, 2017, pp. 1-13, https://doi.org/10.1038/srep42530.

[16] A. N. M. Alahmadi, Design of an Efficient PTB7:PC70BM-Based Polymer Solar Cell for 8% Efficiency", Polymers (Basel), Vol. 14, No. 5, 2022, pp. 889, https://doi.org/10.3390/polym14050889.

[17] W. Li, W. Li, Y. Feng, C. Yang, Numerical Analysis of the Back Interface for High Efficiency Wide Band Gap Chalcopyrite Solar Cells, Sol. Energy, Vol. 180, 2019, pp. 207-215, https://doi.org/10.1016/j.solener.2019.01.018.

[18] A. Mang, K. Reimann, S. Rübenacke, Band Gaps, Crystal-field Splitting, Spin-orbit Coupling, and Exciton Binding Energies in Zno Under Hydrostatic Pressure, Solid State Commun., Vol. 94, No. 4, 1995, pp. 251-254, https://doi.org/10.1016/0038-1098(95)00054-2.

[19] Y. Zhou et al., A Universal Method to Produce Low-Work Function Electrodes for Organic Electronics, Science, Vol. 336, No. 6079, 2012, pp. 327-332, https://doi.org/10.1126/science.1218829.

[20] R. Jaymin et al., PbS-ZnO Solar Cell: A Numerical Simulation, J. Nano-Electron. Phys., Vol. 9, No. 3, 2017, pp. 3041, https://doi.org/10.21272/jnep.9(3).03041.

[21] S. A. J. Thomson, S. C. Hogg, I. D. W. Samuel, D. J. Keeble, Air Exposure Induced Recombination in PTB7:$PC_{71}BM$ Solar Cells, J. Mater. Chem. A, Vol. 5, No. 41, 2017, pp. 21926-21935, https://doi.org/10.1039/c7ta03741d.

[22] M. Mohan et al., Efficient Organic Photovoltaics with Improved Charge Extraction and High Short-Circuit Current, J. Phys. Chem. C, Vol. 121, No. 10, 2017, pp. 5523-5530, https://doi.org/10.1021/acs.jpcc.7b01314.

[23] X. Su et al., Understanding of Photophysical Processes in DIO Additive-treated PTB7:$PC_{71}BM$ Solar Cells, Crystals, Vol. 11, No. 9, 2021, https://doi.org/10.3390/cryst11091139.

[24] Y. Miao, Y. Xu, Y. Zhang, X. Yan, K. Ye, Y. Wang, Constructing Efficient Organic Photovoltaic Devices with A Spirobifluorene Based Water/Alcohol-Soluble Cathode Interlayer, New J. Chem., Vol. 42, No. 11, 2018, pp. 8960-8967, https://doi.org/10.1039/c8nj00807h.

[25] H. Yao et al., Achieving Highly Efficient Nonfullerene Organic Solar Cells with Improved Intermolecular Interaction and Open-Circuit Voltage, Adv. Mater., Vol. 29, No. 21, 2017, pp. 1-8, https://doi.org/10.1002/adma.201700254.

[26] B. Ebenhoch, S. A. J. Thomson, K. Genevičius, G. Juška, I. D. W. Samuel, Charge Carrier Mobility of the Organic Photovoltaic Materials PTB7 and $PC_{71}BM$ and Its Influence on Device Performance, Org. Electron., Vol. 22, 2015, pp. 62-68, https://doi.org/10.1016/j.orgel.2015.03.013.